

# LiSTAR: Ray-Centric World Models for 4D LiDAR Sequences in Autonomous Driving

Pei Liu<sup>1\*†</sup>, Songtao Wang<sup>2\*</sup>, Lang Zhang<sup>2\*‡</sup>, Xingyue Peng<sup>2</sup>, Yuandong Lyu<sup>2</sup>, Jiaxin Deng<sup>2</sup>, Songxin Lu<sup>2</sup>, Weiliang Ma<sup>2</sup>, Xueyang Zhang<sup>2</sup>, Yifei Zhan<sup>2</sup>, XianPeng Lang<sup>2</sup>, Jun Ma<sup>1,3§</sup>

<sup>1</sup>The Hong Kong University of Science and Technology (Guangzhou)

<sup>2</sup>Li Auto Inc.

<sup>3</sup>The Hong Kong University of Science and Technology  
pliu061@connect.hkust-gz.edu.cn, jun.ma@ust.hk

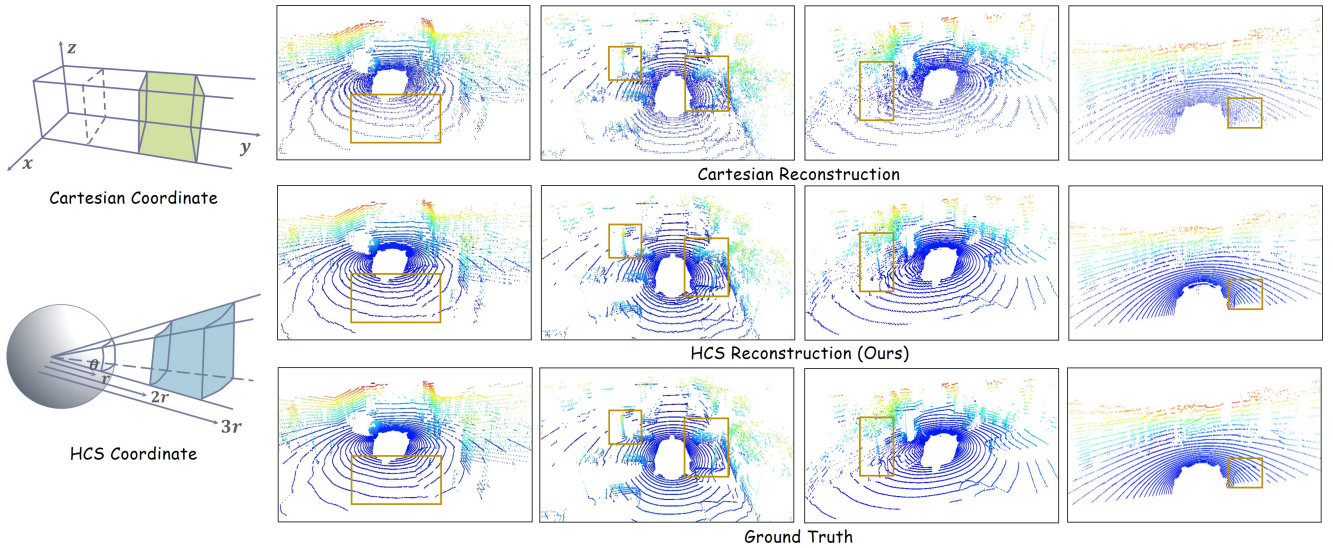


Figure 1. Cartesian vs. HCS coordinate for LiDAR scene representation. Cartesian coordinate partitions space into uniform, axis-aligned cubes, ignoring the native ray geometry of LiDAR. HCS coordinates divides space into angular-radial cells centered at the sensor origin, aligning with LiDAR’s ray-based sampling pattern and preserving range-dependent resolution.

## Abstract

Synthesizing high-fidelity and controllable 4D LiDAR data is crucial for creating scalable simulation environments for autonomous driving. This task is inherently challenging due to the sensor’s unique spherical geometry, the temporal sparsity of point clouds, and the complexity of dynamic scenes. To address these challenges, we present LiSTAR, a novel generative world model that operates directly on the sensor’s native geometry. LiSTAR in-

roduces a Hybrid-Cylindrical-Spherical (HCS) representation to preserve data fidelity by mitigating quantization artifacts common in Cartesian grids. To capture complex dynamics from sparse temporal data, it utilizes a Spatio-Temporal Attention with Ray-Centric Transformer (START) that explicitly models feature evolution along individual sensor rays for robust temporal coherence. Furthermore, for controllable synthesis, we propose a novel 4D point cloud-aligned voxel layout for conditioning and a corresponding discrete Masked Generative START (MaskSTART) framework, which learns a compact, tokenized representation of the scene, enabling efficient, high-resolution, and layout-guided compositional generation. Comprehensive experiments validate LiSTAR’s state-of-the-art performance

\*Equal contribution.

‡Project leader.

§Corresponding author.

†Work done during an internship at Li Auto Inc.

across 4D LiDAR reconstruction, prediction, and conditional generation, with substantial quantitative gains: reducing generation MMD by a massive 76%, improving reconstruction IoU by 32%, and lowering prediction L1 Med by 50%. This level of performance provides a powerful new foundation for creating realistic and controllable autonomous systems simulations. Project link: [LiSTAR](#).

## 1. Introduction

World models, which aim to internalize environmental dynamics by learning generative predictors, have demonstrated strong capabilities across a wide range of visual and interactive tasks and are now increasingly explored for autonomous driving [16, 33]. Recent progress has largely focused on structured modalities like videos and occupancy grids, whose dense organization fits well with established processing pipelines [11, 49]. By contrast, LiDAR remains understudied despite its importance for accurate 3D geometry and all-weather perception. The sparse, unordered, and irregular nature of LiDAR point clouds [21, 29, 55] poses fundamental challenges for generative modeling, limiting the direct adoption of techniques designed for regularly structured data.

Despite recent progress in LiDAR scene synthesis [25, 59, 66], significant hurdles remain. A primary challenge stems from conventional voxelization, which converts LiDAR returns into dense Cartesian grids. As illustrated in Fig. 1, this approach overlooks the native ray-based sampling geometry of spinning sensors, leading to quantization artifacts and distorted structural patterns that impair fidelity [23, 26, 61]. Furthermore, the inherent sparsity and non-uniform sampling of point clouds complicate the preservation of temporal coherence, often resulting in flickering surfaces or inconsistent dynamic object alignment [18]. Finally, for controllable synthesis, the prevalent reliance on temporal Bird’s-Eye-View (BEV) layouts [37, 38] as conditional inputs imposes a critical bottleneck. This 2D projection inherently flattens the rich 3D world, constraining the ability to precisely guide generation or manipulate objects in full 3D space, a capability crucial for targeted scenario design and safety evaluation.

To address these challenges, we introduce LiSTAR, a novel world model built upon a pioneering Hybrid-Cylindrical-Spherical (HCS)-based 4D Vector Quantised-Variational AutoEncoder (VQ-VAE) [3, 48] to learn a discrete representation of LiDAR scenes. LiSTAR begins with a novel HCS representation, the first of its kind for LiDAR world models, which aligns with the sensor’s native scanning geometry to preserve ray structure and mitigate distortions. Building on this representation, our Spatio-Temporal Attention with Ray-Centric Transformer (START) module explicitly models feature correlations along sensor rays

across time, enforcing robust spatial and temporal consistency. Finally, to enable controllable synthesis, we introduce a novel 4D point cloud-aligned voxel layout as a conditioning mechanism. A discrete Masked Generative START (MaskSTART) pipeline then operates on the learned VQ tokens, conditioned on these layouts, to achieve efficient, high-fidelity generation. Collectively, these synergistic innovations enable the creation of 4D LiDAR scenes that are not only physically faithful but also precisely controllable, paving the way for more realistic and targeted autonomous driving simulation.

We conduct extensive experiments on the large-scale nuScenes benchmark, evaluating LiSTAR on a suite of tasks including point cloud reconstruction, prediction, and generation. In both unconditional and layout-conditioned settings, LiSTAR consistently outperforms state-of-the-art baselines. Beyond quantitative metrics, we demonstrate that the framework’s ability to produce controllable, temporally consistent LiDAR sequences unlocks novel downstream applications. The main contributions of this work are:

- We present LiSTAR, a 4D LiDAR world model that unifies HCS representation, START, and MaskSTART into a single end-to-end framework, explicitly tailored to LiDAR’s acquisition geometry and temporal dynamics for world models of autonomous driving.
- We propose an HCS coordinate voxelization scheme that preserves the native ray structure and range resolution, effectively mitigating geometric distortion caused by conventional Cartesian discretization.
- We design the START module, which models feature correlations along LiDAR rays to capture spatial structure and temporal dependencies jointly, ensuring geometric fidelity and frame-to-frame consistency.
- We introduce a MaskSTART pipeline for 4D LiDAR sequences that supports fine-grained semantic conditioning on 4D point cloud-aligned voxel layout. This approach enables controllable and diverse scenario synthesis, allowing for precise manipulation and generation of complex scene structures.
- We achieve state-of-the-art performance on a large-scale autonomous driving benchmark for both point cloud reconstruction, prediction, and generation, and demonstrate LiSTAR’s utility in realistic, controllable simulation scenarios.

## 2. Related Work

### 2.1. 3D Representation for Point Clouds

Choosing an effective 3D representation is critical for point cloud generation. Point-based approaches, such as PointNet and PointNet++ [27, 41, 42], directly operate on raw points, aggregating local and global features to encode spatial context. Voxelization [31, 40, 56] discretizes the space into

dense grids but is memory-intensive, leading to sparse convolution designs [7, 13] that skip empty cells. Projection-based representations are also popular: BEV [22, 56] vertically projects points onto a planar map, while range images [17, 35, 37, 43, 66] map points to polar coordinates to form 2.5D grids. Recent works leverage VAE-family models [10, 20, 48] for latent compression, e.g., VQ-VAE [3, 48] learns discrete codebooks for compact feature tokens. For simulation, ray-casting pipelines [2, 9, 32, 36] reproduce ray-drop patterns from virtual assets. Finally, implicit neural representations, such as NeRF [34], allow differentiable rendering of point clouds from learned occupancy or semantic fields [23, 60].

## 2.2. World Models for Point Clouds

World models predict future observations from historical states and agent actions, enabling agents to model temporal dynamics. While early work focused on image/video prediction [16, 45, 53, 62, 63], recent studies extend to structured 3D data. In 3D occupancy world models [14, 24, 50, 64, 65], discrete volumetric tokens are predicted to maintain spatial consistency. Point cloud world models [57, 61, 67] predict temporal LiDAR sequences by combining latent tokenization and generative backbones. For instance, Copilot4D [61] encodes LiDAR frames with VQ-VAE and applies discrete diffusion for forecasting, while LiDAR-DM [67] adapts diffusion transformers for long-horizon predictions. These approaches highlight the promise and current limitations of scalable, geometry-aware token-based generative modeling for 4D LiDAR.

## 2.3. Diffusion Models

Diffusion models learn a forward process that progressively corrupts data with noise, and a reverse process to recover the original signal. For continuous data, Gaussian perturbations [15, 44, 46, 47] are widely used due to favorable statistical properties enabling stable training objectives. MaskGIT [5] replaces Gaussian noise with aggressive token masking and BERT-style training [8], outperforming Gaussian diffusion in several domains, including video [58] and point clouds [54]. Beyond diffusion, flow matching [28] learns continuous-time flows between base and target distributions, allowing ODE-based sampling with convergence guarantees, and has been applied to sequences [12] and spatial modalities. Recent works adapt these generative paradigms to 3D point clouds, using token-based pipelines, view-consistent constraints, and geometry-aware noise schedules to improve spatial fidelity and temporal stability, making them promising backbones for LiDAR world modeling.

## 3. Methodology

We introduce LiSTAR, a novel generative world model for 4D LiDAR synthesis, composed of two synergistic components: an HCS-based 4D VQ-VAE for representation learning and a MaskSTART model for prediction and generation.

The HCS-based 4D VQ-VAE, shown in Fig. 2 (left), first transforms the input LiDAR sequence into a compact, discrete latent space. The encoder employs stacked START blocks, featuring Spatial Ray-Centric Attention (SRA) and Cyclic-Shifted Temporal Causal Attention (CSTA), to capture spatio-temporal dynamics and produce a quantized codebook representation effectively. This discrete representation then serves as the foundation for the MaskSTART model (Fig. 2, right), a unified framework that performs masked generative modeling for both prediction and conditional generation. In the generation task, it conditions on 4D point cloud-aligned voxel layouts, which are fused via a zero-initialized adapter to guide the synthesis of realistic and semantically consistent sequences. Further details on the algorithmic procedures for reconstruction, prediction, and generation are provided in the Appendix.

### 3.1. HCS Coordinate Voxelization

Conventional Cartesian voxelization forces a trade-off between fidelity and efficiency: high-resolution grids needed for detail are massively sparse and computationally expensive. We overcome this by proposing a voxelization scheme in an HCS Coordinate System that mirrors the native spherical projection of LiDAR sensors, as shown in Fig. 1. Our method partitions space into bins of constant angular resolution, preserving geometric details at all ranges while yielding a compact and efficient representation. Formally, a point cloud is defined as:

$$P = \{\mathbf{p}^{(n)} \in \mathbb{R}^3 \mid 1 \leq n \leq N\},$$

where each point  $\mathbf{p}^{(n)} = (x^{(n)}, y^{(n)}, z^{(n)})$  is expressed in Cartesian coordinate. We map these points into the HCS coordinate system  $(\rho^{(n)}, \theta^{(n)}, \phi^{(n)})$  using:

$$\begin{cases} \rho^{(n)} = \sqrt{(x^{(n)})^2 + (y^{(n)})^2}, \\ \theta^{(n)} = \arctan 2(y^{(n)}, x^{(n)}), \\ \phi^{(n)} = \arctan 2(z^{(n)}, \rho^{(n)}). \end{cases} \quad (1)$$

The voxelization is performed by a function  $V : (\rho, \theta, \phi) \rightarrow (i, j, k)$ , which quantizes a point’s continuous HCS coordinates into a discrete integer tuple. This tuple  $(i, j, k)$  indexes a specific bin within a 3D grid along the radial, angular, and axial dimensions. The final output is a binary occupancy grid  $\mathcal{G}$ , where an element  $\mathcal{G}_{i,j,k} = 1$  if the corresponding voxel is non-empty, and 0 otherwise. This formulation provides a structured and compact encoding of the raw point cloud, ideal for consumption by subsequent network layers.

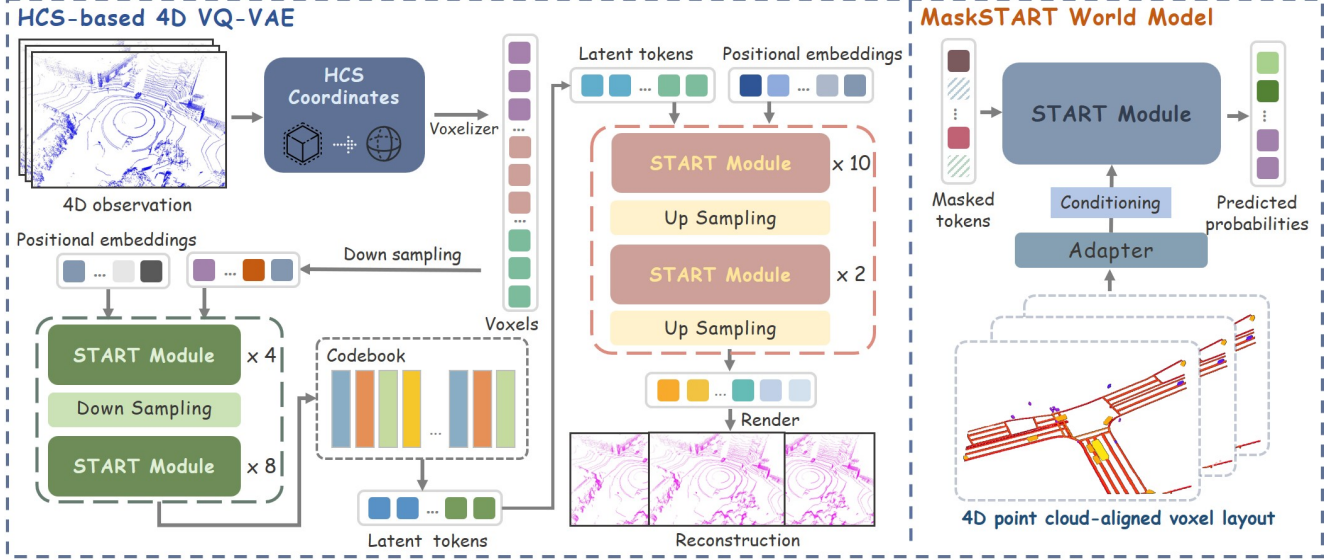


Figure 2. Illustration of the LiSTAR framework for 4D LiDAR sequence reconstruction and generation. The framework begins by voxelizing LiDAR point clouds into a spherical coordinate representation, which is downsampled and processed by multiple START modules in the encoder to extract semantic-rich latent tokens. The decoder reconstructs detailed 4D sequences by up-sampling tokens with additional START modules. The MaskSTART component facilitates controllable and diverse generation by predicting masked tokens using a bidirectional transformer, conditioned on 4D point cloud-aligned voxel layouts. This design captures spatiotemporal dependencies while preserving fine-grained geometric details.

### 3.2. START Module

We introduce the START module, a novel 4D attention mechanism specifically designed for sequential LiDAR data. START operates in a causal temporal manner to capture motion patterns while leveraging spatial ray-centric attention, explicitly aligned with the intrinsic geometry of LiDAR sensors. This formulation enables the model to capture both spatiotemporal dependencies and fine-grained structural relationships effectively, as illustrated in Fig. 3.

#### 3.2.1. Spatial Ray-Centric Attention

To explicitly encode the intrinsic ray-like structure of LiDAR scans, we introduce the Ray-Centric Attention (RA) layer. It operates on a dense tensor  $V_{\rho\theta\phi} \in \mathbb{R}^{l \times h \times w}$ , where  $l$ ,  $h$ , and  $w$  correspond to the ray, vertical, and horizontal angular dimensions, respectively. To efficiently process this representation, we first unfold (F) the tensor  $V$  along its ray dimension  $l$ , transforming it into a 2D matrix of size  $d \times l$ , where  $d = h \times w$ . A standard self-attention mechanism is then applied to a normalized version of this flattened representation, denoted  $V_n$ . The output is computed as:

$$V_n = \text{Norm}(F(V)), \quad (2)$$

$$V' = \text{softmax} \left( \frac{V_n W_Q (V_n W_K)^T}{\sqrt{d_k}} \right) V_n W_V, \quad (3)$$

where  $W_Q$ ,  $W_K$ , and  $W_V$  are linear projection matrices that map the input features into query, key, and value spaces.

This mechanism enables each ray to aggregate information from all other rays based on their learned similarities, effectively capturing the global context of the 3D scene.

Spatial RA (SRA) block embeds the proposed RA layer within a pre-norm Transformer architecture. The process involves a residual connection after the RA-layer, followed by Layer Normalization (LN) and a Feed-Forward Network (FFN) with a second residual connection. Formally, this is expressed as:

$$V_{\text{SRA}} = F^{-1} ((V' + f(V')) + g(\text{LN}(V' + f(V')))), \quad (4)$$

where  $f(\cdot)$  and  $g(\cdot)$  represent the RA layer and the FFN, respectively.  $F^{-1}$  indicates the inverse function of  $F$ . This residual-in-residual design ensures stable training while enhancing feature expressiveness.

Applying standard self-attention to the full 4D voxel grid is not only computationally prohibitive but also structurally agnostic to the underlying LiDAR geometry. It fails to exploit the inherent radial dependencies captured by sensor rays. Our SRA addresses this by restricting attention computations to the radial dimension. This targeted approach allows the model to efficiently reason about occlusions and spatial relationships along each line of sight. Consequently, SRA captures fine-grained local structures while maintaining global context, all within a feasible computational budget.

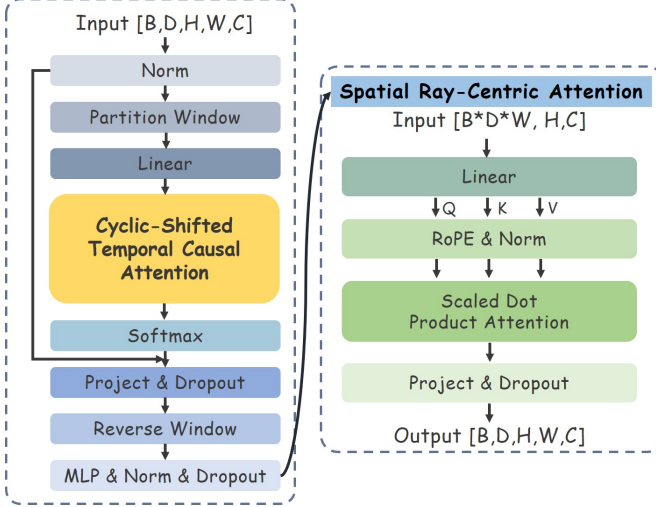


Figure 3. An illustration of our START module. It processes a 4D feature map of shape  $[B, D, H, W, C]$ , where  $D$  is the temporal dimension. It is composed of two key components: (1) a CSTA block that operates on windowed features to efficiently model temporal dependencies, and (2) an SRA block that processes features reshaped to  $[B * D, H, W, C]$  to capture spatial correlations along the ray dimension.

### 3.2.2. Cyclic-Shifted Temporal Causal Attention

To effectively model 4D LiDAR sequences, our model must address two fundamental challenges: the spatial discontinuity arising from spherical coordinate projection, and the need for causal temporal modeling. To this end, we propose the CSTA module, which is composed of two specialized mechanisms. First, Cyclic-Shifted Window Attention (CSWA) restores spatial continuity across the azimuthal seam by leveraging a shifted-windowing scheme inspired by the Swin Transformer [30]. Second, Temporal Causal Attention (TCA) enforces a strict chronological order to learn valid motion patterns without information leakage from the future.

**Cyclic-Shifted Window Attention.** The projection of LiDAR’s HCS coordinates onto a discrete grid introduces a critical spatial discontinuity. Points that are physically adjacent across the azimuthal seam ( $0^\circ/360^\circ$ ) are placed at opposite ends of the tensor’s width dimension, artificially severing their geometric relationship.

This issue can be conceptualized by considering the mapping of a local neighborhood. Let  $\mathcal{N}(p)$  denote a connected 3D neighborhood of a point  $p$  located on the azimuthal boundary. The projection onto a tensor of width  $W$  splits this single neighborhood into two disjoint sets of indices at the extremes of the tensor dimension:

$$\mathcal{N}(p) \xrightarrow{\text{Projection}} \dots, w_{W-2}, w_{W-1} \cup w_0, w_1, \dots. \quad (5)$$

Consequently, standard network operators with fixed recep-

tive fields (e.g., convolutions, window attention) fail to process this neighborhood cohesively. They perceive the two parts as maximally distant, leading to feature artifacts and an incomplete understanding of the global scene structure.

---

#### Algorithm 1 Cyclic-Shifted Window Attention (CSWA)

---

**Input:** Input feature map  $X_l \in \mathbb{R}^{B \times D \times H \times W \times C}$  from layer  $l$ , window size  $(M_D, M_H, M_W)$ .

**Output:** Output feature map  $X_{l+1}$  from the subsequent layer.

- 1:       ▷ **Stage 1: Standard Window MSA (W-MSA)**
  - 2:  $X' \leftarrow \text{LayerNorm}(X_l)$
  - 3:  $X_{\text{windows}} \leftarrow \text{WindowPartition}(X', (M_D, M_H, M_W))$  ▷ Partition into non-overlapping windows
  - 4:  $A_{\text{windows}} \leftarrow \text{MSA}(X_{\text{windows}})$        ▷ Apply Multi-Head Self-Attention within each window
  - 5:  $A \leftarrow \text{WindowReverse}(A_{\text{windows}}, (D, H, W))$  ▷ Merge windows back
  - 6:  $X_l \leftarrow X_l + A$                        ▷ First residual connection
  - 7:  $X_l \leftarrow X_l + \text{MLP}(\text{LayerNorm}(X_l))$  ▷ Second residual connection with MLP
  
  - 8:       ▷ **Stage 2: Shifted Window MSA (SW-MSA)**
  - 9:  $X'' \leftarrow \text{LayerNorm}(X_l)$
  - 10:  $X_{\text{shifted}} \leftarrow \text{CyclicShift}(X'', (M_D/2, M_H/2, M_W/2))$  ▷ Cyclic shift along the azimuthal (W) dimension
  - 11:       ▷ Generate mask to prevent attention between non-adjacent regions
  - 12:  $M \leftarrow \text{GenerateMask}(D, H, W, (M_D, M_H, M_W))$
  - 13:  $X'_{\text{windows}} \leftarrow \text{WindowPartition}(X_{\text{shifted}}, (M_D, M_H, M_W))$
  - 14:  $A'_{\text{windows}} \leftarrow \text{MSA}(X'_{\text{windows}}, \text{mask} = M)$        ▷ Apply MSA with the generated mask
  - 15:  $A'_{\text{shifted}} \leftarrow \text{WindowReverse}(A'_{\text{windows}}, (D, H, W))$
  - 16:  $A' \leftarrow \text{CyclicShift}(A'_{\text{shifted}}, (0, 0, M_W/2))$  ▷ Reverse the cyclic shift
  - 17:  $X_{l+1} \leftarrow X_l + A'$                    ▷ Third residual connection
  - 18:  $X_{l+1} \leftarrow X_{l+1} + \text{MLP}(\text{LayerNorm}(X_{l+1}))$  ▷ Fourth residual connection with MLP
  - 19: **return**  $X_{l+1}$
- 

To address the boundary discontinuity induced by spherical coordinate unwrapping, we propose CSWA. CSWA explicitly models the periodic nature of the azimuthal dimension, enabling information flow across the artificial seam. The mechanism operates in two alternating stages. The procedure, detailed in Alg. 1, alternates between two configurations. A standard Window MSA (W-MSA) first computes self-attention within local, non-overlapping windows for efficient feature extraction. Subsequently, a Shifted Window MSA (SW-MSA) block introduces a cyclic shift along the azimuthal dimension. This realigns the window grid, enabling cross-window connections, particularly across the

Table 1. **LiSTAR significantly outperforms the previous state-of-the-art method in point cloud reconstruction.** Our method demonstrates significant improvements across all metrics, achieving a 32% relative increase in IoU and a 60% reduction in MMD, indicating superior geometric accuracy and distribution similarity. Best results are in bold. (↑: Higher is better, ↓: Lower is better).

Method	IoU↑	Chamfer↓	MMD ( $10^{-4}$ )↓	JSD↓
OpenDWM [1, 6, 39]	0.441	0.029	0.152	0.076
Ours	<b>0.583</b> (32%↑)	<b>0.017</b> (41%↓)	<b>0.061</b> (60%↓)	<b>0.056</b> (26%↓)

Table 2. **LiSTAR sets a new state-of-the-art in point cloud prediction.** The table compares our method with previous state-of-the-art approaches on the nuScenes dataset. LiSTAR achieves a 17% reduction in Chamfer distance and a 50% reduction in L1 Med. Metrics shown in blue are evaluated within a  $\pm 70$ m ROI. Best results are in bold. ↓ indicates lower is better.

Method	Chamfer↓	L1 Med↓	AbsRel Med↓	L1 Mean↓	AbsRel↓
SPFNet [51]	2.24	-	-	4.58	34.87
S2Net [52]	1.70	-	-	3.49	28.38
4D-Occ [19]	1.41	0.26	4.02	1.40	10.37
Copilot4D [61]	0.36	0.10	1.30	1.30	8.58
Ours	<b>0.30</b> (17%↓)	<b>0.05</b> (50%↓)	<b>0.96</b> (26%↓)	<b>0.76</b> (42%↓)	<b>4.92</b> (43%↓)

$0^\circ/360^\circ$  seam. A carefully designed attention mask ensures that interactions are confined to valid local regions in the shifted configuration before the shift is reversed.

By alternating these standard and shifted window configurations, CSWA achieves a global receptive field with linear complexity, efficiently restoring the topological continuity of the spherical space.

**Temporal Causal Attention.** Beyond static spatial features, modeling temporal dynamics is crucial for interpreting motion and ensuring coherence across LiDAR frames. Standard attention mechanisms are permutation-invariant and thus non-causal, allowing information to leak from future frames, which is invalid for predictive tasks.

To address this, we introduce TCA, a mechanism designed to model scene evolution while strictly adhering to the arrow of time. TCA extends the causal constraint to a history of  $L$  preceding frames,  $\{X_{t-L}, X_{t-L+1}, \dots, X_{t-1}\}$ , allowing the model to capture long-range temporal dependencies. Queries  $Q_t$  are generated from the current frame  $X_t$ , while a unified set of keys  $K_{hist}$  and values  $V_{hist}$  is created by concatenating the respective projections from all  $L$  past frames. The attention mechanism then aggregates information from the entire history as follows:

$$\text{TCA}(X_t) = \text{softmax} \left( \frac{Q_t K_{hist}^T}{\sqrt{d_k}} \right) V_{hist}. \quad (6)$$

This formulation ensures that the model’s output for time  $t$  depends on past and present information, enabling it to learn robust and complex motion patterns from a rich temporal context.

We integrate TCA by interleaving it with CSWA layers.

This layered structure allows the model to jointly refine spatial details and update temporal states, creating a comprehensive 4D representation. This unified approach is essential for tasks requiring both spatial integrity and temporal coherence, such as dynamic scene reconstruction and motion forecasting.

## 4. Experiments

In this section, we aim to conduct experiments to investigate the following questions: (1) Does LiSTAR achieve state-of-the-art performance on the autonomous driving benchmark across point cloud reconstruction, forecasting, and generation tasks? (2) How crucial are the respective contributions of the HCS representation and the START module? (3) Qualitatively, how effective is LiSTAR at generating temporally coherent and high-fidelity reconstructions?

### 4.1. Datasets and Experiment Setting

Our experiments are conducted on the large-scale nuScenes dataset [4], which provides dense, 360-degree point clouds from a 128-beam LiDAR. We utilize the official train/val split, focusing on keyframes from diverse urban scenarios. To create a fixed-size input, each raw point cloud is down-sampled to 2048 points via Farthest Point Sampling (FPS). For the prediction task, we define the operational range as  $[-70, 70]$ m in x/y and  $[-4.5, 4.5]$ m in z, while for the generation task, the range is  $[-50, 50]$ m in x/y and  $[-3, 5]$ m in z. All models are trained for 60k steps on 64 H20 GPUs using the AdamW optimizer with a learning rate of  $5e-5$ . We use a per-GPU batch size of 2 and train with bf16 precision for computational efficiency.

Table 3. **LiSTAR demonstrates superior performance in LiDAR generation.** Our method significantly outperforms the OpenDWM baseline in both geometric accuracy and distributional fidelity. As shown, LiSTAR reduces the MMD by 76% and cuts the Chamfer distance by over 50% across different evaluation ranges: 30m (magenta), 40m (green), and 70m (blue). This highlights our model’s ability to generate significantly more realistic and accurate point cloud sequences. Best results are in bold.

Method	Chamfer $\downarrow$	Chamfer $\downarrow$	Chamfer $\downarrow$	MMD ( $10^{-4}$ ) $\downarrow$	JSD $\downarrow$
OpenDWM	1.88	2.57	3.35	41.14	0.31
Ours	<b>0.72</b> (62% $\downarrow$ )	<b>1.21</b> (53% $\downarrow$ )	<b>1.53</b> (54% $\downarrow$ )	<b>9.94</b> (76% $\downarrow$ )	<b>0.30</b>

Table 4. **Our proposed HCS coordinate achieves superior performance.** The table presents a direct comparison against standard Cartesian and Polar coordinates, where our method demonstrates significant gains across all metrics. For example, it boosts IoU by 16% over the next-best polar representation. Bold denotes the best performance.

Cartesian	Polar	HCS	IoU $\uparrow$	Chamfer $\downarrow$	MMD ( $10^{-4}$ ) $\downarrow$	JSD $\downarrow$
✓			0.414	0.039	0.475	0.086
	✓		0.476	0.023	0.072	0.067
		✓	<b>0.554</b> (16% $\uparrow$ )	<b>0.020</b> (13% $\downarrow$ )	<b>0.065</b> (10% $\downarrow$ )	<b>0.060</b> (10% $\downarrow$ )

## 4.2. Metrics

To comprehensively evaluate our method, LiSTAR, across point cloud reconstruction, prediction, and generation, we assess both per-sample geometric fidelity and overall distributional similarity. For geometric fidelity, we measure volumetric accuracy using Intersection over Union (IoU) and quantify point-wise discrepancies using Chamfer distance, L1 distance (both Mean and Median), and Absolute Relative error (AbsRel). Notably, for the LiDAR generation task, Chamfer distance is evaluated across multiple ranges (30m, 40m, and 70m) to assess fidelity at varying distances. To evaluate the distributional quality of the generated set, we employ Maximum Mean Discrepancy (MMD) and Jensen-Shannon Divergence (JSD), which are critical for judging the realism and diversity of the generated point cloud sequences.

## 4.3. Reconstruction Results

As shown in Table 1, LiSTAR significantly outperforms the previous state-of-the-art method, OpenDWM, in the task of point cloud reconstruction. Our method achieves substantial gains across the board, with a 26% relative increase in IoU and a 57% reduction in MMD. These results demonstrate that LiSTAR not only reconstructs scene geometry more accurately by achieving a higher IoU and lower Chamfer Distance, but also captures the data distribution with much higher fidelity, reflected in lower MMD and JSD. This comprehensive improvement validates the effectiveness of our proposed architecture for high-quality reconstruction.

## 4.4. Prediction Results

The results for 1 s future prediction are presented in Table 2. Our method, LiSTAR, significantly outperforms all base-

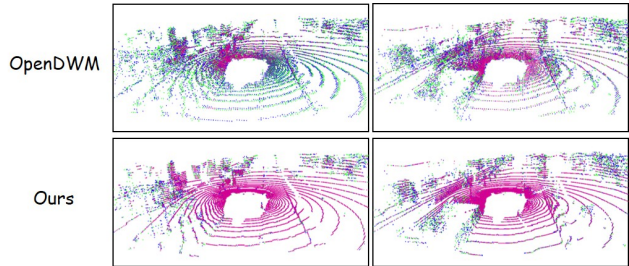


Figure 4. Qualitative comparison of point cloud reconstruction. The visualization overlays predictions with the ground truth: magenta (correct intersection), green (missed ground truth), and blue (artifacts). Our method consistently yields more complete reconstructions (denser magenta) with significantly fewer artifacts (less blue), demonstrating superior accuracy.

lines, establishing a new state-of-the-art. Notably, for the 1s future horizon, LiSTAR reduces the Chamfer distance by 17% and the L1 Med by a remarkable 50% compared to Copilot4D. This comprehensive improvement at the 1 s horizon validates the effectiveness of our architecture in producing highly accurate and reliable future predictions.

## 4.5. Generation Results

For the LiDAR generation task, we compare LiSTAR with the OpenDWM baseline, presenting quantitative results in Table 3. Our method demonstrates a substantial advantage across all metrics. Most notably, LiSTAR achieves a remarkable 76% reduction in Maximum Mean Discrepancy (MMD), indicating that the distribution of our generated point clouds is significantly closer to the ground truth. In terms of geometric accuracy, our model consistently reduces the Chamfer distance by over 50% across all evalu-

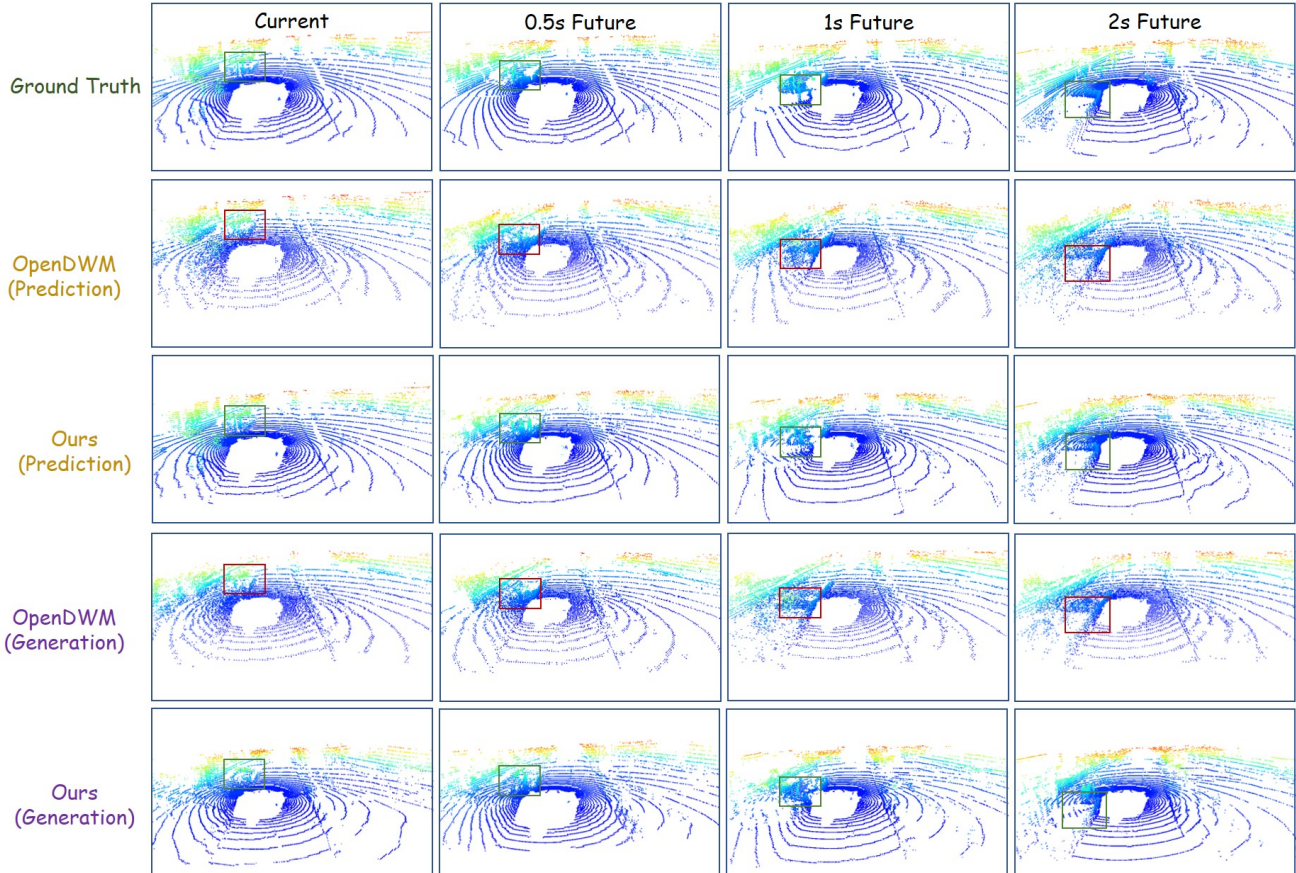


Figure 5. Qualitative results for prediction and generation. We compare our method with OpenDWM against the ground truth for future horizons up to 2s. Our method consistently produces sharper and more accurate results for both static background and dynamic objects (highlighted) compared to the baseline. The baseline’s predictions and generations degrade significantly over time, losing structural detail.

ated ranges: 30m (magenta), 40m (green), and 70m (blue). These results collectively validate the superior capability of our model in generating high-fidelity and physically realistic LiDAR sequences.

## 4.6. Ablation Study

### 4.6.1. Analysis of Coordinate Representation

Table 4 presents our ablation study on coordinate systems, demonstrating the clear superiority of our proposed HCS representation. HCS substantially outperforms both Cartesian and the stronger Polar coordinate baselines across all metrics. Specifically, it achieves an IoU of 0.554, marking a significant 16% relative improvement over Polar coordinates. This result strongly validates the advantage of HCS in providing a more powerful representation for LiDAR data.

### 4.6.2. Effectiveness of the START Module

Table 5 validates the synergistic design of our START module, demonstrating that both SRA and CSTA are critical for performance. The introduction of SRA alone provides

Table 5. **Combining attention mechanisms in START yields superior performance.** The table ablates our two attention mechanisms, showing that each provides a substantial gain over the baseline. Their combination in the START module is most effective, for instance, improving IoU from 0.503 to 0.583. Bold denotes the best performance.

SRA	CSTA	IoU $\uparrow$	Chamfer $\downarrow$	MMD ( $10^{-4}$ ) $\downarrow$	JSD $\downarrow$
		0.503	0.021	0.116	0.061
✓		0.554	0.020	0.065	0.060
✓	✓	<b>0.583</b>	<b>0.017</b>	<b>0.061</b>	<b>0.056</b>

the most significant leap, dramatically improving IoU from 0.503 to 0.554 and slashing the MMD from 0.116 to 0.065. The subsequent addition of CSTA further enhances performance across all metrics, leading to the best overall scores, including a final IoU of 0.583. This clearly shows that while SRA captures the core geometric structure, CSTA is essential for achieving the highest level of temporal and distributional fidelity.

## 4.7. Qualitative Results

Our qualitative results in Fig. 4 and 5 demonstrate LiSTAR’s clear superiority across all tasks. In reconstruction, the baseline accumulates significant artifacts (blue points) over time, while our method maintains high fidelity with more true positives (magenta). Similarly, for prediction and generation, the baseline’s outputs become progressively blurry and lose structural detail, whereas our results remain sharp and temporally consistent, closely matching the ground truth. This visual evidence confirms our model’s advanced capability in modeling complex 4D dynamics with high fidelity. Further experimental details are provided in the Appendix.

## 5. Conclusion

In this paper, we introduced LiSTAR, a novel generative world model for high-fidelity, controllable 4D LiDAR synthesis. By unifying a novel HCS representation with a START, LiSTAR effectively preserves geometric fidelity and ensures temporal coherence. Its discrete MaskSTART framework further enables efficient, high-resolution generation conditioned on scene layouts. We have demonstrated that LiSTAR establishes a new state-of-the-art across reconstruction, prediction, and generation tasks, providing a powerful tool for creating realistic simulation environments for autonomous driving. Future work could explore multi-modal conditioning for even richer scene synthesis.

## References

- [1] Opendwm: Open driving world models, 2025. <https://github.com/SenseTime-FVG/OpenDWM>. 6
- [2] Alexander Amini, Tsun-Hsuan Wang, Igor Gilitschenski, Wilko Schwarting, Zhijian Liu, Song Han, Sertac Karaman, and Daniela Rus. VISTA 2.0: An Open, Data-driven Simulator for Multimodal Sensing and Policy Learning for Autonomous Vehicles. In *2022 International Conference on Robotics and Automation (ICRA)*, pages 2419–2426, 2022. 3
- [3] Lucas Caccia, Herke Van Hoof, Aaron Courville, and Joelle Pineau. Deep Generative Modeling of LiDAR Data. In *2019 IEEE/RSJ International Conference on Intelligent Robots and Systems (IROS)*, pages 5034–5040, 2019. 2, 3
- [4] Holger Caesar, Varun Bankiti, Alex H Lang, Sourabh Vora, Venice Erin Liong, Qiang Xu, Anush Krishnan, Yu Pan, Giancarlo Baldan, and Oscar Beijbom. nuScenes: A Multimodal Dataset for Autonomous Driving. In *Proceedings of the IEEE/CVF conference on computer vision and pattern recognition*, pages 11621–11631, 2020. 6
- [5] Huiwen Chang, Han Zhang, Lu Jiang, Ce Liu, and William T Freeman. MaskGIT: Masked Generative Image Transformer. In *Proceedings of the IEEE/CVF conference on computer vision and pattern recognition*, pages 11315–11325, 2022. 3
- [6] Rui Chen, Zehuan Wu, Yichen Liu, Yuxin Guo, Jingcheng Ni, Haifeng Xia, and Siyu Xia. Unimlvg: Unified framework for multi-view long video generation with comprehensive control capabilities for autonomous driving. *arXiv preprint arXiv:2412.04842*, 2024. 6
- [7] Christopher B Choy, Danfei Xu, JunYoung Gwak, Kevin Chen, and Silvio Savarese. 3D-R2N2: A Unified Approach for Single and Multi-view 3D Object Reconstruction. In *European conference on computer vision*, pages 628–644, 2016. 3
- [8] Jacob Devlin, Ming-Wei Chang, Kenton Lee, and Kristina Toutanova. BERT: Pre-training of Deep Bidirectional Transformers for Language Understanding. In *Proceedings of the 2019 conference of the North American chapter of the association for computational linguistics: human language technologies, volume 1 (long and short papers)*, pages 4171–4186, 2019. 3
- [9] Alexey Dosovitskiy, German Ros, Felipe Codevilla, Antonio Lopez, and Vladlen Koltun. CARLA: An Open Urban Driving Simulator. In *Conference on robot learning*, pages 1–16, 2017. 3
- [10] Patrick Esser, Robin Rombach, and Bjorn Ommer. Taming Transformers for High-Resolution Image Synthesis. In *Proceedings of the IEEE/CVF conference on computer vision and pattern recognition*, pages 12873–12883, 2021. 3
- [11] Ruiyuan Gao, Kai Chen, Enze Xie, Lanqing Hong, Zhen-guo Li, Dit-Yan Yeung, and Qiang Xu. MagicDrive: Street View Generation with Diverse 3D Geometry Control. *arXiv preprint arXiv:2310.02601*, 2023. 2
- [12] Zhengyang Geng, Mingyang Deng, Xingjian Bai, J Zico Kolter, and Kaiming He. Mean Flows for One-step Generative Modeling. *arXiv preprint arXiv:2505.13447*, 2025. 3
- [13] Benjamin Graham, Martin Engelcke, and Laurens Van Der Maaten. 3D Semantic Segmentation With Submanifold Sparse Convolutional Networks. In *Proceedings of the IEEE conference on computer vision and pattern recognition*, pages 9224–9232, 2018. 3
- [14] Songen Gu, Wei Yin, Bu Jin, Xiaoyang Guo, Junming Wang, Haodong Li, Qian Zhang, and Xiaoxiao Long. DOME: Taming Diffusion Model into High-Fidelity Controllable Occupancy World Model. *arXiv preprint arXiv:2410.10429*, 2024. 3
- [15] Jonathan Ho, Ajay Jain, and Pieter Abbeel. Denoising Diffusion Probabilistic Models. *Advances in neural information processing systems*, 33:6840–6851, 2020. 3
- [16] Anthony Hu, Lloyd Russell, Hudson Yeo, Zak Murez, George Fedoseev, Alex Kendall, Jamie Shotton, and Gianluca Corrado. GAIA-1: A Generative World Model for Autonomous Driving. *arXiv preprint arXiv:2309.17080*, 2023. 2, 3
- [17] Qianjiang Hu, Zhimin Zhang, and Wei Hu. RangeLDM: Fast Realistic LiDAR Point Cloud Generation. In *European Conference on Computer Vision*, pages 115–135, 2024. 3
- [18] Ziqi Huang, Yanan He, Jiashuo Yu, Fan Zhang, Chenyang Si, Yuming Jiang, Yuanhan Zhang, Tianxing Wu, Qingyang Jin, Nattapol Chanpaisit, et al. VBench: Comprehensive Benchmark Suite for Video Generative Models. In *Proceedings of the IEEE/CVF Conference on Computer Vision and Pattern Recognition*, pages 21807–21818, 2024. 2
- [19] Tarasha Khurana, Peiyun Hu, David Held, and Deva Ramanan. Point Cloud Forecasting as a Proxy for 4D Occupancy Forecasting. In *Proceedings of the IEEE/CVF Conference on Computer Vision and Pattern Recognition*, pages 1116–1124, 2023. 6
- [20] Diederik P Kingma and Max Welling. Auto-Encoding Variational Bayes. *arXiv preprint arXiv:1312.6114*, 2013. 3
- [21] Lingdong Kong, Youquan Liu, Xin Li, Runnan Chen, Wenwei Zhang, Jiawei Ren, Liang Pan, Kai Chen, and Ziwei Liu. Robo3D: Towards Robust and Reliable 3D Perception against Corruptions. In *Proceedings of the IEEE/CVF International Conference on Computer Vision*, pages 19994–20006, 2023. 2
- [22] Alex H Lang, Sourabh Vora, Holger Caesar, Lubing Zhou, Jiong Yang, and Oscar Beijbom. PointPillars: Fast Encoders for Object Detection From Point Clouds. In *Proceedings of the IEEE/CVF conference on computer vision and pattern recognition*, pages 12697–12705, 2019. 3
- [23] Bohan Li, Jiazhe Guo, Hongsi Liu, Yingshuang Zou, Yikang Ding, Xiwu Chen, Hu Zhu, Feiyang Tan, Chi Zhang, Tiancai Wang, et al. UniScene: Unified Occupancy-centric Driving Scene Generation. In *Proceedings of the Computer Vision and Pattern Recognition Conference*, pages 11971–11981, 2025. 2, 3
- [24] Heng Li, Yuenan Hou, Xiaohan Xing, Yuexin Ma, Xiao Sun, and Yanyong Zhang. OccMamba: Semantic Occupancy Prediction with State Space Models. In *Proceedings of the Computer Vision and Pattern Recognition Conference*, pages 11949–11959, 2025. 3
- [25] Jiang Li, Jinhao Liu, and Qingqing Huang. PointDMM: A Deep-Learning-Based Semantic Segmentation Method for

- Point Clouds in Complex Forest Environments. *Forests*, 14 (12):2276, 2023. 2
- [26] Ao Liang, Youquan Liu, Yu Yang, Dongyue Lu, Linfeng Li, Lingdong Kong, Huaici Zhao, and Wei Tsang Ooi. LiDARCrafter: Dynamic 4D World Modeling from LiDAR Sequences. *arXiv preprint arXiv:2508.03692*, 2025. 2
- [27] Zhouhan Lin, Minwei Feng, Cicero Nogueira dos Santos, Mo Yu, Bing Xiang, Bowen Zhou, and Yoshua Bengio. A Structured Self-attentive Sentence Embedding. *arXiv preprint arXiv:1703.03130*, 2017. 2
- [28] Yaron Lipman, Ricky TQ Chen, Heli Ben-Hamu, Maximilian Nickel, and Matt Le. Flow Matching for Generative Modeling. *arXiv preprint arXiv:2210.02747*, 2022. 3
- [29] Youquan Liu, Lingdong Kong, Jun Cen, Runnan Chen, Wenwei Zhang, Liang Pan, Kai Chen, and Ziwei Liu. Segment Any Point Cloud Sequences by Distilling Vision Foundation Models. *Advances in Neural Information Processing Systems*, 36:37193–37229, 2023. 2
- [30] Ze Liu, Yutong Lin, Yue Cao, Han Hu, Yixuan Wei, Zheng Zhang, Stephen Lin, and Baining Guo. Swin Transformer: Hierarchical Vision Transformer Using Shifted Windows. In *Proceedings of the IEEE/CVF international conference on computer vision*, pages 10012–10022, 2021. 5
- [31] Zhijian Liu, Haotian Tang, Shengyu Zhao, Kevin Shao, and Song Han. PVNAS: 3D Neural Architecture Search With Point-Voxel Convolution. *IEEE Transactions on Pattern Analysis and Machine Intelligence*, 44(11):8552–8568, 2021. 2
- [32] Sivabalan Manivasagam, Shenlong Wang, Kelvin Wong, Wenyuan Zeng, Mikita Sazanovich, Shuhan Tan, Bin Yang, Wei-Chiu Ma, and Raquel Urtasun. LiDARsim: Realistic LiDAR Simulation by Leveraging the Real World. In *Proceedings of the IEEE/CVF Conference on Computer Vision and Pattern Recognition*, pages 11167–11176, 2020. 3
- [33] Jianbiao Mei, Tao Hu, Xuemeng Yang, Licheng Wen, Yu Yang, Tiantian Wei, Yukai Ma, Min Dou, Botian Shi, and Yong Liu. DreamForge: Motion-Aware Autoregressive Video Generation for Multi-View Driving Scenes. *arXiv preprint arXiv:2409.04003*, 2024. 2
- [34] Ben Mildenhall, Pratul P Srinivasan, Matthew Tancik, Jonathan T Barron, Ravi Ramamoorthi, and Ren Ng. NeRF: Representing Scenes as Neural Radiance Fields for View Synthesis. *Communications of the ACM*, 65(1):99–106, 2021. 3
- [35] Andres Milioto, Ignacio Vizzo, Jens Behley, and Cyrill Stachniss. RangeNet ++: Fast and Accurate LiDAR Semantic Segmentation. In *2019 IEEE/RSJ international conference on intelligent robots and systems (IROS)*, pages 4213–4220, 2019. 3
- [36] Kazuto Nakashima and Ryo Kurazume. Learning to Drop Points for LiDAR Scan Synthesis. In *2021 IEEE/RSJ International Conference on Intelligent Robots and Systems (IROS)*, pages 222–229, 2021. 3
- [37] Kazuto Nakashima and Ryo Kurazume. LiDAR Data Synthesis with Denoising Diffusion Probabilistic Models. In *2024 IEEE International Conference on Robotics and Automation (ICRA)*, pages 14724–14731, 2024. 2, 3
- [38] Kazuto Nakashima, Xiaowen Liu, Tomoya Miyawaki, Yumi Iwashita, and Ryo Kurazume. Fast LiDAR Data Generation with Rectified Flows. In *2025 IEEE International Conference on Robotics and Automation (ICRA)*, pages 10057–10063. IEEE, 2025. 2
- [39] Jingcheng Ni, Yuxin Guo, Yichen Liu, Rui Chen, Lewei Lu, and Zehuan Wu. Maskgwm: A generalizable driving world model with video mask reconstruction. *arXiv preprint arXiv:2502.11663*, 2025. 6
- [40] Charles R Qi, Hao Su, Matthias Nießner, Angela Dai, Mengyuan Yan, and Leonidas J Guibas. Volumetric and Multi-View CNNs for Object Classification on 3D Data. In *Proceedings of the IEEE conference on computer vision and pattern recognition*, pages 5648–5656, 2016. 2
- [41] Charles R Qi, Hao Su, Kaichun Mo, and Leonidas J Guibas. PointNet: Deep Learning on Point Sets for 3D Classification and Segmentation. In *Proceedings of the IEEE conference on computer vision and pattern recognition*, pages 652–660, 2017. 2
- [42] Charles Ruizhongtai Qi, Li Yi, Hao Su, and Leonidas J Guibas. PointNet++: Deep Hierarchical Feature Learning on Point Sets in a Metric Space. *Advances in neural information processing systems*, 30, 2017. 2
- [43] Haoxi Ran, Vitor Guizilini, and Yue Wang. Towards Realistic Scene Generation with LiDAR Diffusion Models. In *Proceedings of the IEEE/CVF Conference on Computer Vision and Pattern Recognition*, pages 14738–14748, 2024. 3
- [44] Robin Rombach, Andreas Blattmann, Dominik Lorenz, Patrick Esser, and Björn Ommer. High-Resolution Image Synthesis With Latent Diffusion Models. In *Proceedings of the IEEE/CVF conference on computer vision and pattern recognition*, pages 10684–10695, 2022. 3
- [45] Lloyd Russell, Anthony Hu, Lorenzo Bertoni, George Fedoseev, Jamie Shotton, Elahe Arani, and Gianluca Corrado. GAIA-2: A Controllable Multi-View Generative World Model for Autonomous Driving. *arXiv preprint arXiv:2503.20523*, 2025. 3
- [46] Jiaming Song, Chenlin Meng, and Stefano Ermon. Denoising Diffusion Implicit Models. *arXiv preprint arXiv:2010.02502*, 2020. 3
- [47] Yang Song, Jascha Sohl-Dickstein, Diederik P Kingma, Abhishek Kumar, Stefano Ermon, and Ben Poole. Score-Based Generative Modeling through Stochastic Differential Equations. *arXiv preprint arXiv:2011.13456*, 2020. 3
- [48] Aaron Van Den Oord, Oriol Vinyals, et al. Neural Discrete Representation Learning. *Advances in neural information processing systems*, 30, 2017. 2, 3
- [49] Lening Wang, Wenzhao Zheng, Yilong Ren, Han Jiang, Zhiyong Cui, Haiyang Yu, and Jiwen Lu. OccSora: 4D Occupancy Generation Models as World Simulators for Autonomous Driving. *arXiv preprint arXiv:2405.20337*, 2024. 2
- [50] Julong Wei, Shanshuai Yuan, Pengfei Li, Qingda Hu, Zhongxue Gan, and Wenchao Ding. OccLLaMA: An Occupancy-Language-Action Generative World Model for Autonomous Driving. *arXiv preprint arXiv:2409.03272*, 2024. 3

- [51] Xinshuo Weng, Jianren Wang, Sergey Levine, Kris Kitani, and Nicholas Rhinehart. Inverting the Pose Forecasting Pipeline with SPF2: Sequential Pointcloud Forecasting for Sequential Pose Forecasting. In *Conference on robot learning*, pages 11–20. PMLR, 2021. 6
- [52] Xinshuo Weng, Junyu Nan, Kuan-Hui Lee, Rowan McAllister, Adrien Gaidon, Nicholas Rhinehart, and Kris M Kitani. S2Net: Stochastic Sequential Pointcloud Forecasting. In *European Conference on Computer Vision*, pages 549–564. Springer, 2022. 6
- [53] Wei Wu, Xi Guo, Weixuan Tang, Tingxuan Huang, Chiyu Wang, Dongyue Chen, and Chenjing Ding. DriveScape: Towards High-Resolution Controllable Multi-View Driving Video Generation. *arXiv preprint arXiv:2409.05463*, 2024. 3
- [54] Yuwen Xiong, Wei-Chiu Ma, Jingkang Wang, and Raquel Urtasun. Learning Compact Representations for LiDAR Completion and Generation. In *Proceedings of the IEEE/CVF Conference on Computer Vision and Pattern Recognition*, pages 1074–1083, 2023. 3
- [55] Xiang Xu, Lingdong Kong, Hui Shuai, Wenwei Zhang, Liang Pan, Kai Chen, Ziwei Liu, and Qingshan Liu. 4D Contrastive Superflows are Dense 3D Representation Learners. In *European Conference on Computer Vision*, pages 58–80. Springer, 2024. 2
- [56] Bin Yang, Wenjie Luo, and Raquel Urtasun. PIXOR: Real-Time 3D Object Detection From Point Clouds. In *Proceedings of the IEEE conference on Computer Vision and Pattern Recognition*, pages 7652–7660, 2018. 2, 3
- [57] Zetong Yang, Li Chen, Yanan Sun, and Hongyang Li. Visual Point Cloud Forecasting enables Scalable Autonomous Driving. In *Proceedings of the IEEE/CVF Conference on Computer Vision and Pattern Recognition*, pages 14673–14684, 2024. 3
- [58] Lijun Yu, Yong Cheng, Kihyuk Sohn, José Lezama, Han Zhang, Huiwen Chang, Alexander G Hauptmann, Ming-Hsuan Yang, Yuan Hao, Irfan Essa, et al. MAGVIT: Masked Generative Video Transformer. In *Proceedings of the IEEE/CVF Conference on Computer Vision and Pattern Recognition*, pages 10459–10469, 2023. 3
- [59] Sihyun Yu, Kihyuk Sohn, Subin Kim, and Jinwoo Shin. Video Probabilistic Diffusion Models in Projected Latent Space. In *Proceedings of the IEEE/CVF conference on computer vision and pattern recognition*, pages 18456–18466, 2023. 2
- [60] Junge Zhang, Feihu Zhang, Shaochen Kuang, and Li Zhang. NeRF-LiDAR: Generating Realistic LiDAR Point Clouds with Neural Radiance Fields. In *Proceedings of the AAAI Conference on Artificial Intelligence*, pages 7178–7186, 2024. 3
- [61] Lunjun Zhang, Yuwen Xiong, Ze Yang, Sergio Casas, Rui Hu, and Raquel Urtasun. Copilot4D: Learning Unsupervised World Models for Autonomous Driving via Discrete Diffusion. *arXiv preprint arXiv:2311.01017*, 2023. 2, 3, 6
- [62] Guosheng Zhao, Chaojun Ni, Xiaofeng Wang, Zheng Zhu, Xueyang Zhang, Yida Wang, Guan Huang, Xinze Chen, Boyuan Wang, Youyi Zhang, et al. DriveDreamer4D: World Models Are Effective Data Machines for 4D Driving Scene Representation. In *Proceedings of the Computer Vision and Pattern Recognition Conference*, pages 12015–12026, 2025. 3
- [63] Guosheng Zhao, Xiaofeng Wang, Zheng Zhu, Xinze Chen, Guan Huang, Xiaoyi Bao, and Xingang Wang. DriveDreamer-2: LLM-Enhanced World Models for Diverse Driving Video Generation. In *Proceedings of the AAAI Conference on Artificial Intelligence*, pages 10412–10420, 2025. 3
- [64] Wenzhao Zheng, Weiliang Chen, Yuanhui Huang, Borui Zhang, Yueqi Duan, and Jiwen Lu. OccWorld: Learning a 3D Occupancy World Model for Autonomous Driving. In *European conference on computer vision*, pages 55–72, 2024. 3
- [65] Sicheng Zuo, Wenzhao Zheng, Yuanhui Huang, Jie Zhou, and Jiwen Lu. GaussianWorld: Gaussian World Model for Streaming 3D Occupancy Prediction. In *Proceedings of the Computer Vision and Pattern Recognition Conference*, pages 6772–6781, 2025. 3
- [66] Vlas Zyrianov, Xiyue Zhu, and Shenlong Wang. Learning to Generate Realistic LiDAR Point Clouds. In *European Conference on Computer Vision*, pages 17–35, 2022. 2, 3
- [67] Vlas Zyrianov, Henry Che, Zhijian Liu, and Shenlong Wang. LidarDM: Generative LiDAR Simulation in a Generated World. In *2025 IEEE International Conference on Robotics and Automation (ICRA)*, pages 6055–6062, 2025. 3

# LiSTAR: Ray-Centric World Models for 4D LiDAR Sequences in Autonomous Driving

## Supplementary Material

### 6. Methodology

#### 6.1. HCS-based 4D VQ-VAE

To capture both geometric structures and temporal dynamics inherent in sequential LiDAR scans, we design a VQ-VAE tailored to the 4D HCS voxel representation. This framework effectively abstracts redundant measurements while preserving crucial spatiotemporal information, enabling reconstruction, future sequence prediction and generation. The framework consists of a hierarchical encoder that maps the input sequence to a discrete latent space and a generative decoder that reconstructs the 4D volume from this representation.

##### 6.1.1. Hierarchical Encoder

The encoder  $E$ , detailed in Alg. 2, transforms the input sequence  $\mathbf{x} \in \mathbb{R}^{\rho \times \theta \times \phi \times T}$  into a compact latent representation  $\mathbf{z} = E(\mathbf{x}) \in \mathbb{R}^{x \times x \times x \times D}$ . This process begins with spherical coordinate voxelization to obtain voxel features  $\{v_1, v_2, \dots, v_N\}$ , which addresses the non-uniform distribution problem inherent to point clouds across varying viewing angles and distances. The voxel feature encoding employs our CSTA module for comprehensive cross-dimensional interaction, allowing features to be processed across both spatial and temporal domains. Subsequently, the SRA module enhances feature correlations among voxels along shared laser-ray directions, fostering coherent representation.

Inspired by video generation advances, our 4D-VAE model enables unified spatiotemporal processing, avoiding frame-by-frame limitations that often compromise temporal consistency. Encoding involves patch merging of voxels, followed by the application of four stacked START blocks to extract spatiotemporal features. A  $2 \times 2 \times 1$  downsampling operation is applied, reducing feature representation by a factor of  $8 \times 8 \times 2$  in polar BEV space. Further encoding proceeds through START blocks without ray-specific attention, ultimately generating a robust latent space  $z \in \mathbb{R}^{X \times X \times X \times D}$ , which undergoes vector quantization yielding  $\hat{z} \in \mathcal{C}$ , where  $\mathcal{C}$  is the codebook of latent vectors.

##### 6.1.2. Generative Decoder

The decoder  $D$  reconstructs the LiDAR volume from the quantized latent representation  $\hat{z} \in \mathcal{C}$ , as outlined in Alg. 3, producing  $\tilde{\mathbf{x}} = D(\hat{z}) \in \mathbb{R}^{\rho \times \theta \times \phi \times T}$ , ensuring both geometric fidelity and temporal coherence. Initial processing leverages eight STA blocks without Ray Attention for fea-

---

#### Algorithm 2 Encoder of HCS-based 4D VQ-VAE

---

**Input:** Input voxelized LiDAR sequence  $V \in \mathbb{R}^{\rho \times \theta \times \phi \times T}$ .  
**Output:** Latent representation  $z \in \mathbb{R}^{H' \times W' \times D' \times C'}$ .

- 1:  $h \leftarrow \text{PatchMerge}(V)$   $\triangleright$  Initial patch merging of voxels
- 2: **for**  $i = 1 \rightarrow 4$  **do**  $\triangleright$  Apply four stacked START blocks for spatiotemporal feature extraction
- 3:      $h \leftarrow \text{START\_Block}_i(h)$
- 4: **end for**
- 5:  $h \leftarrow \text{Downsample}_{2 \times 2 \times 1}(h)$   $\triangleright$  Reduce spatial resolution
- 6: **for**  $i = 1 \rightarrow K$  **do**  $\triangleright$  Further encoding with CSTA blocks
- 7:      $h \leftarrow \text{CSTA\_Block}_i(h)$
- 8: **end for**
- 9:  $z \leftarrow h$   $\triangleright$  Final latent representation
- 10: **return**  $z$

---

ture restoration, followed by a  $2 \times 2 \times 1$  upsampling operation. Next, two START blocks refine spatiotemporal information and depth cues along ray directions, reinforcing structural integrity and continuity within the reconstructed output. The features are then upsampled back to the original voxel size, with the final point cloud  $\tilde{\mathcal{P}} = \{\tilde{p}_1, \tilde{p}_2, \dots, \tilde{p}_M\}$  rendered by a dedicated module, ensuring consistent geometry and smooth motion trajectories.

##### 6.1.3. Loss Function

The encoder-decoder framework is trained by minimizing a loss function with three components: vector quantization loss, voxel reconstruction loss, and point cloud reconstruction loss:

$$L = L_{VQ}(z, \hat{z}) + L_v(V_{pred}, V_{target}) + L_p(U_{pred}, V_{target}), \quad (7)$$

where  $z$  and  $\hat{z}$  are encoder outputs and quantized features, respectively;  $V_{pred}$  denotes the predicted voxels,  $U_{pred}$  represents voxelized rendered point cloud; and  $V_{target}$  denotes target voxels. This loss formulation ensures fidelity across both voxel representation and rendered point clouds, enhancing reconstruction quality.

### 6.2. MaskSTART Module

We present the MaskSTART Module, a comprehensive framework designed for both point cloud prediction and generation tasks. Illustrated in Fig. 6, this module excels in generating future LiDAR sequences  $\{\tilde{\mathcal{P}}_{t+1}, \dots, \tilde{\mathcal{P}}_{t+\tau}\}$

---

**Algorithm 3** Decoder of HCS-based 4D VQ-VAE

---

**Input:** Quantized latent representation  $\hat{z} \in \mathbb{R}^{H' \times W' \times D' \times C'}$ .

**Output:** Reconstructed voxel volume  $V_{\text{out}}$  and point cloud  $\tilde{\mathcal{P}}$ .

```
1:  $h' \leftarrow \hat{z}$   $\triangleright$  Start decoding from quantized latent
2: for  $i = 1 \rightarrow 8$  do  $\triangleright$  Initial feature restoration with STA blocks
3:    $h' \leftarrow \text{STA\_Block}_i(h')$ 
4: end for
5:  $h' \leftarrow \text{Upsample}_{2 \times 2 \times 1}(h')$   $\triangleright$  Increase spatial resolution
6: for  $i = 1 \rightarrow 2$  do  $\triangleright$  Refine with START blocks to reinforce ray structure
7:    $h' \leftarrow \text{START\_Block}_i(h')$ 
8: end for
9:  $V_{\text{out}} \leftarrow \text{Upsample}(h')$   $\triangleright$  Upsample to original voxel resolution
10:  $\tilde{\mathcal{P}} \leftarrow \text{RenderModule}(V_{\text{out}})$   $\triangleright$  Render final point cloud from voxels
11: return  $V_{\text{out}}, \tilde{\mathcal{P}}$ 
```

---

from past observations  $\{\mathcal{P}_{t-\tau+1}, \dots, \mathcal{P}_t\}$  while incorporating various conditional inputs for generation, such as scene layouts, textual descriptions, or visual cues.

Initially, the method aligns raw point cloud coordinates  $\mathcal{P}_t = \{p_i\}_{i=1}^M$  with the LiDAR’s inherent geometric distribution through conversion to spherical coordinates  $(\rho, \theta, \phi)$ , followed by voxelization into a grid  $\mathbf{x}_t \in \mathbb{R}^{\rho \times \theta \times \phi}$ . A tokenizer  $T(\cdot)$  then maps the voxel grid into a discrete token sequence  $\mathbf{s}_t = T(\mathbf{x}_t)$ , which is processed by a MaskSTART module for masked generative tasks under differing conditional settings.

### 6.2.1. Regional Spatiotemporal Attention

The MaskSTART module integrates  $N$  stacked Transformer blocks designed to address spatiotemporal inconsistencies arising from the motion of the ego-vehicle and dynamic objects. These inconsistencies can compromise the temporal coherence of generated point clouds in long sequences.

To effectively capture long-range dependencies and resolve these issues, we introduce Regional Spatio-Temporal Attention (RSTA). Unlike conventional attention mechanisms that compute attention scores across all tokens  $\mathbf{s}_t = \{s_{t,1}, \dots, s_{t,M}\}$ , RSTA predicts offsets  $\Delta_{t,i}$  for each token  $s_{t,i}$  to locate regions of interest (RoIs)  $\mathcal{R}_{t,i} \subseteq \mathbf{s}_{\leq t}$ , facilitating attention computation exclusively within these targeted areas. This selective approach efficiently models spatiotemporal variations while minimizing computational overhead.

RSTA maintains strict causality by preserving the chronological progression of events, ensuring predictions rely solely on past and present information. This causal framework, paired with the 3D Swin Transformer’s Tempo-

ral Attention, provides enhanced temporal consistency and spatial fidelity in point cloud sequences, making RSTA particularly suited for handling dynamic environments.

### 6.2.2. Prediction Task

In prediction tasks, the model takes as input a sequence of historical observations  $\{h^1, \dots, h^t\}$ , where each observation  $h^t = \{o^t, c^t\}$  consists of LiDAR point cloud data  $o^t$  and associated conditional information  $c^t$  (e.g., ego-vehicle pose). The goal of the model is to learn a probabilistic world model  $p_\theta$  capable of predicting future point clouds conditioned on the historical context. During training, as detailed in Alg. 4, the model encodes the input point cloud sequence using an hierarchical encoder to extract latent features. Historical frames are encoded and serve as the conditional input, while future frame tokens are processed with a masking strategy to improve robustness and generation accuracy. Specifically, tokens in future frames are either randomly replaced with other tokens from the codebook, assigned learnable mask tokens, or left unaltered. The MaskSTART module learns to infer the masked tokens based on the given historical sequence, optimizing the following loss function:

$$L_{\text{CE}} = - \sum_{i \in \mathcal{M}} \log p(z_{q,i} | z'_q) \quad (8)$$

$L_{\text{CE}}$  is the total Cross-Entropy loss.  $\mathcal{M}$  is the set of indices corresponding to all masked token positions in the future sequence. The loss is computed exclusively over these positions.  $z_{q,i}$  is the ground-truth token (i.e., the correct codebook index) at position  $i$ .  $z'_q$  is the masked input sequence provided to the MaskSTART module, which consists of the historical context and the corrupted future sequence.  $p(z_{q,i} | z'_q)$  is the predicted probability.

Alg. 5 outlines the inference procedure. The encoded features of the historical frames serve as conditional input, while future frames are initialized with mask tokens. The MaskSTART module synthesizes future frames iteratively. In each iteration, the model predicts the probability distribution over the codebook for all masked positions, samples tokens for high-confidence positions, and re-masks low-confidence tokens to refine subsequent generation steps. This iterative refinement process continues until the entire token sequence is generated. To enhance the quality of the output, a mask scheduling strategy is employed. During the early stages of inference, the generation of the most frequent tokens (often corresponding to background classes, such as ground or sky) is suppressed, encouraging the model to prioritize the generation of key scene elements like vehicles and pedestrians. Additionally, classifier-free guidance (CFG) is employed to balance diversity and conditional accuracy during generation. This is formulated as:

$$z' = z^c + \gamma \times (z^c - z^u) \quad (9)$$

---

**Algorithm 4** Training for Prediction with MaskSTART

---

**Input:** Historical observation sequence  $O_{\text{hist}} = \{o^1, \dots, o^t\}$ .  
**Input:** Future observation sequence  $O_{\text{future}} = \{o^{t+1}, \dots, o^T\}$ .  
**Input:** Encoder  $E$ , Codebook  $\mathcal{C}$ , MaskSTART module  $M_{\text{START}}$ .  
**Output:** Trained parameters for  $M_{\text{START}}$ .

- 1:  $\triangleright$  1. Encode full sequence and get ground-truth tokens
- 2:  $O_{\text{full}} \leftarrow \text{Concat}(O_{\text{hist}}, O_{\text{future}})$
- 3:  $z \leftarrow E(O_{\text{full}})$   $\triangleright$  Encode to get latent features
- 4:  $z_q \leftarrow \text{VectorQuantize}(z, \mathcal{C})$   $\triangleright$  Get discrete ground-truth tokens
- 5:  $z_{q,\text{hist}}, z_{q,\text{future}} \leftarrow \text{Split}(z_q)$   $\triangleright$  Split into history and future tokens
- 6:  $\triangleright$  2. Apply masking strategy to future tokens
- 7:  $M \leftarrow \text{GenerateRandomMask}(z_{q,\text{future}})$   $\triangleright$  Create a boolean mask for future tokens
- 8:  $z'_{q,\text{future}} \leftarrow \text{ApplyMaskingStrategy}(z_{q,\text{future}}, M)$   $\triangleright$  Replace, mask, or keep tokens
- 9:  $\triangleright$  3. Predict masked tokens
- 10:  $z'_{q,\text{input}} \leftarrow \text{Concat}(z_{q,\text{hist}}, z'_{q,\text{future}})$   $\triangleright$  Combine history and masked future
- 11:  $\text{logits} \leftarrow M_{\text{START}}(z'_{q,\text{input}})$   $\triangleright$  Predict logits for the entire sequence
- 12:  $\triangleright$  4. Calculate loss on masked positions
- 13:  $L_{\text{ce}} \leftarrow \text{CrossEntropyLoss}(\text{logits}[M], z_{q,\text{future}}[M])$   $\triangleright$  Loss only on masked future tokens
- 14: **return**  $L_{\text{ce}}$

---

where  $z^c$  is the conditionally generated output,  $z^u$  is the unconditionally generated output (with historical conditions removed), and  $\gamma$  is the guidance coefficient controlling the trade-off between consistency and diversity.

### 6.2.3. Generation Task

For generation tasks, which is summarized in Alg. 6, the model generates new point cloud sequences conditioned on scene layouts  $\{P^1, \dots, P^T\}$ , without relying on historical point clouds. Each layout encodes the structural composition of the scene, providing a semantic blueprint for synthesis. To maximize the utility of layout information, the scene layout is represented explicitly in a 3D voxel space, as opposed to common top-down 2D representations. This 3D representation preserves height information, improving the model’s ability to control the vertical positioning of objects, such as road signs and traffic lights, capabilities that are inherently limited in 2D layouts. After the layout is converted to spherical coordinates, its features are extracted using an N-layer adapter network. These layout features are then fused with voxelized point cloud features via element-wise addition using a zero convolution layer, ensuring that

---

**Algorithm 5** Iterative Inference for Prediction with MaskSTART

---

**Input:** Historical observation sequence  $O_{\text{hist}}$ , number of generation steps  $N_{\text{iter}}$ , guidance scale  $\gamma$ .  
**Output:** Predicted future token sequence  $\hat{z}_{q,\text{future}}$ .

- 1:  $\triangleright$  1. Initialize with historical context and masked future
- 2:  $z_{q,\text{hist}} \leftarrow \text{VectorQuantize}(E(O_{\text{hist}}))$
- 3:  $\hat{z}_{q,\text{future}} \leftarrow \text{InitializeWithMasks}(\text{length} = T - t)$   $\triangleright$  Create a sequence of [MASK] tokens
- 4: **for**  $k = 1 \rightarrow N_{\text{iter}}$  **do**
- 5:  $\triangleright$  2. Predict logits with Classifier-Free Guidance
- 6:  $c \leftarrow z_{q,\text{hist}}$   $\triangleright$  Conditional context
- 7:  $u \leftarrow \text{null\_context}$   $\triangleright$  Unconditional context (e.g., empty sequence)
- 8:  $\text{logits}_c \leftarrow M_{\text{START}}(\text{Concat}(c, \hat{z}_{q,\text{future}}))$
- 9:  $\text{logits}_u \leftarrow M_{\text{START}}(\text{Concat}(u, \hat{z}_{q,\text{future}}))$
- 10:  $\text{logits} \leftarrow \text{logits}_u + \gamma \times (\text{logits}_c - \text{logits}_u)$   $\triangleright$  Apply CFG
- 11:  $\triangleright$  3. Apply mask scheduling
- 12:  $\text{logits} \leftarrow \text{ApplyMaskScheduling}(\text{logits}, k)$   $\triangleright$  Suppress background tokens in early steps
- 13:  $\text{probs} \leftarrow \text{Softmax}(\text{logits})$
- 14:  $\triangleright$  4. Sample high-confidence tokens and re-mask others
- 15:  $\text{confidences} \leftarrow \max(\text{probs}, \text{dim} = -1)$
- 16:  $\text{mask\_to\_keep} \leftarrow \text{GetHighConfidenceMask}(\text{confidences}, k)$
- 17:  $\text{new\_tokens} \leftarrow \text{Sample}(\text{probs})$
- 18:  $\hat{z}_{q,\text{future}}[\text{mask\_to\_keep}] \leftarrow \text{new\_tokens}[\text{mask\_to\_keep}]$   $\triangleright$  Update confident tokens
- 19: **end for**
- 20: **return**  $\hat{z}_{q,\text{future}}$

---

the layout information is seamlessly integrated without disrupting the backbone network during early training stages.

The fused features are passed to the MaskSTART module for conditional generation. Similar to the prediction task, masked tokens in the sequence are iteratively refined through scheduled decoding until the final point cloud sequence is produced. By leveraging the explicit 3D layout structure, the model generates highly realistic point cloud sequences that preserve geometric fidelity, temporal coherence, and semantic consistency.

The MaskSTART Module offers a unified framework for prediction and generation tasks, leveraging the discrete latent space and masked generative modeling to produce accurate and diverse LiDAR sequence outputs. Its ability to condition on historical observations or external layout information enables it to adapt to various real-world scenarios, including long-sequence prediction and controlled scene generation.

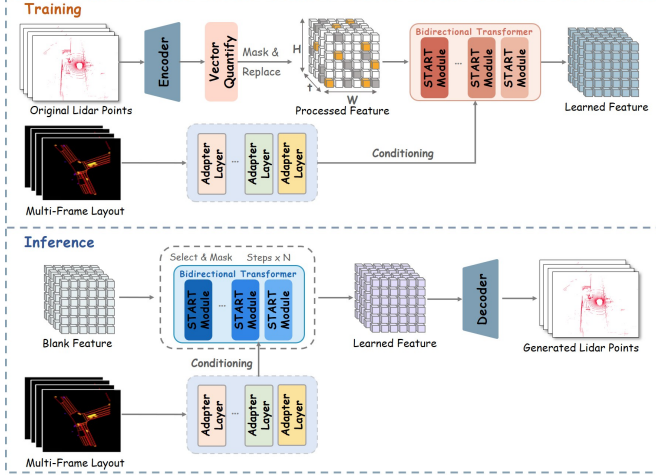


Figure 6. Generation training and inference

## 7. More Experiments

### 7.1. Qualitative Results

Fig. 7 presents a qualitative comparison of our method against the OpenDWM baseline for point cloud reconstruction across two distinct sequences. The visualization overlays reconstructions with the ground truth, where magenta indicates the correct intersection (true positives), green denotes missed ground truth (false negatives), and blue highlights reconstruction artifacts (false positives). The results visually underscore the superior performance of our approach. The outputs from OpenDWM become progressively noisy and incomplete over time, accumulating significant false positives (blue artifacts) while failing to capture the full geometry. In stark contrast, our method consistently produces more complete reconstructions, evidenced by a denser volume of true positives (magenta), and maintains this high fidelity across all time steps from 0s to 3s. This demonstrates our model’s enhanced ability to robustly integrate temporal information without the significant error accumulation that plagues the baseline, validating its superior accuracy and robustness.

Fig. 8 provides a qualitative comparison of our method against the OpenDWM baseline for future LiDAR prediction and generation. The results visually underscore the superior fidelity and noise handling of our approach. The outputs from OpenDWM suffer from significant noise, particularly in the far-field, where it hallucinates numerous scattered points. Furthermore, its representation of near-field objects becomes progressively blurry and loses structural integrity over time. In stark contrast, our method generates much cleaner sequences, effectively suppressing far-field noise while maintaining a dense and geometrically accurate representation of near-field objects. As highlighted in the figure, our model consistently produces sharp, well-defined

---

### Algorithm 6 Conditional Generation from 4D Layouts

---

**Input:** 4D scene layout sequence  $L_{4D} = \{L^1, \dots, L^T\}$ .

**Input:** Number of iterative generation steps  $N_{iter}$ .

**Input:** Models: Adapter, MaskSTART, Decoder  $D$ , RenderModule.

**Output:** Generated point cloud sequence  $\tilde{\mathcal{P}}$ .

---

```

1:                                     ▷ 1. Process 4D Conditional Layout
2:  $V_{layouts} \leftarrow \text{Voxelize3D}(L_{4D})$  ▷ Voxelize the sequence
   of 3D layouts
3:  $V_{layouts\_hcs} \leftarrow \text{ConvertToHCS}(V_{layouts})$  ▷ Convert the
   4D volume to HCS
4:  $F_{layouts} \leftarrow \text{AdapterNetwork}(V_{layouts\_hcs})$  ▷ Extract 4D
   layout features

5:                                     ▷ 2. Initialize Generation
6:  $\hat{z}_q \leftarrow \text{InitializeWithMasks}(\text{length} = T)$  ▷ Create a 4D
   canvas of [MASK] tokens

7:                                     ▷ 3. Iterative Refinement using MaskSTART
8: for  $k = 1 \rightarrow N_{iter}$  do
9:   ▷ Fuse 4D layout features with current token
   embeddings
10:   $E_{tokens} \leftarrow \text{GetEmbeddings}(\hat{z}_q)$  ▷ Get embeddings
   for the current token sequence
11:   $E_{fused} \leftarrow E_{tokens} + \text{ZeroConv}(F_{layouts})$  ▷
   Element-wise fusion across the 4D volume
12:   ▷ Predict logits for masked positions
13:   $\text{logits} \leftarrow M_{\text{START}}(E_{fused})$ 
14:   ▷ Apply scheduled decoding
15:   $\text{probs} \leftarrow \text{Softmax}(\text{ApplyMaskScheduling}(\text{logits}, k))$ 
16:   ▷ Sample high-confidence tokens and re-mask
   others
17:   $\text{confidences} \leftarrow \max(\text{probs}, \text{dim} = -1)$ 
18:   $\text{mask\_to\_keep} \leftarrow$ 
    $\text{GetHighConfidenceMask}(\text{confidences}, k)$ 
19:   $\text{new\_tokens} \leftarrow \text{Sample}(\text{probs})$ 
20:   $\hat{z}_q[\text{mask\_to\_keep}] \leftarrow \text{new\_tokens}[\text{mask\_to\_keep}]$  ▷
   Update confident tokens
21: end for

22:                                     ▷ 4. Decode Final Token Sequence
23:  $V_{gen} \leftarrow D(\hat{z}_q)$  ▷ Decode the completed 4D token
   sequence
24:  $\tilde{\mathcal{P}} \leftarrow \text{RenderModule}(V_{gen})$  ▷ Render the final point
   cloud sequence
25: return  $\tilde{\mathcal{P}}$ 

```

---

structures that closely match the ground truth, demonstrating a superior ability to model complex 4D dynamics with both high fidelity and robustness to noise.

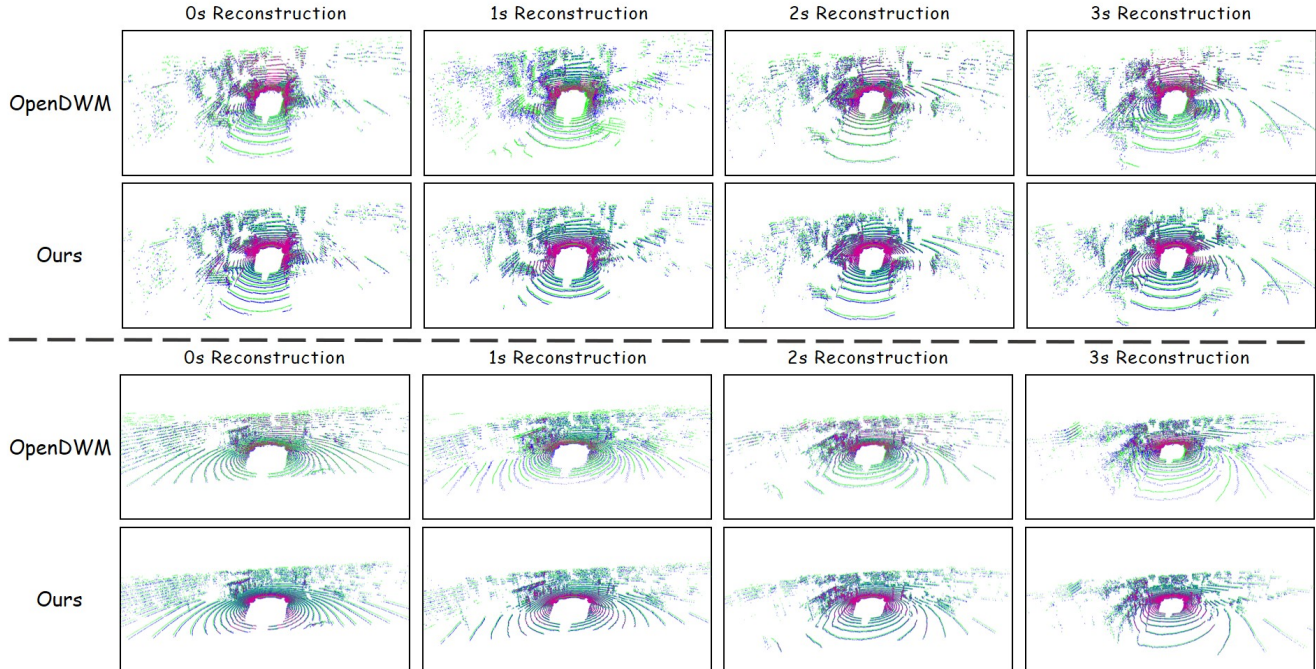


Figure 7. Qualitative comparison of point cloud reconstruction. We compare our method against the OpenDWM baseline on two distinct sequences (top and bottom sections) for time horizons of 0s, 1s, 2s, and 3s. The visualization overlays reconstructions with the ground truth: magenta indicates the correct intersection (true positives), green denotes missed ground truth (false negatives), and blue highlights reconstruction artifacts (false positives). Our method consistently produces more complete reconstructions (denser magenta) and significantly fewer artifacts (less blue) across all time steps, demonstrating superior reconstruction accuracy and robustness.

## 7.2. Limitations

Despite the strong performance of LiSTAR, we acknowledge several limitations that present opportunities for future work. First, our HCS representation is specifically tailored to the geometry of spinning LiDARs. This specialization, while effective, may limit its direct applicability to other 3D sensor modalities, such as solid-state LiDARs or depth cameras, which feature different sampling patterns. Second, as a VQ-VAE-based model, LiSTAR is subject to inherent quantization error, where fine-grained details can be lost during the discretization of the latent space. Furthermore, the iterative refinement process of the MaskSTART module, while crucial for high-quality synthesis, incurs higher computational latency during inference compared to single-pass generative models, which could be a consideration for real-time applications. Finally, our controllable generation relies on the availability of detailed 4D point cloud-aligned voxel layouts, which may not always be accessible in all scenarios. Future research could focus on developing more universal representations, exploring faster generative paradigms, and enabling more abstract forms of conditioning, such as natural language commands.

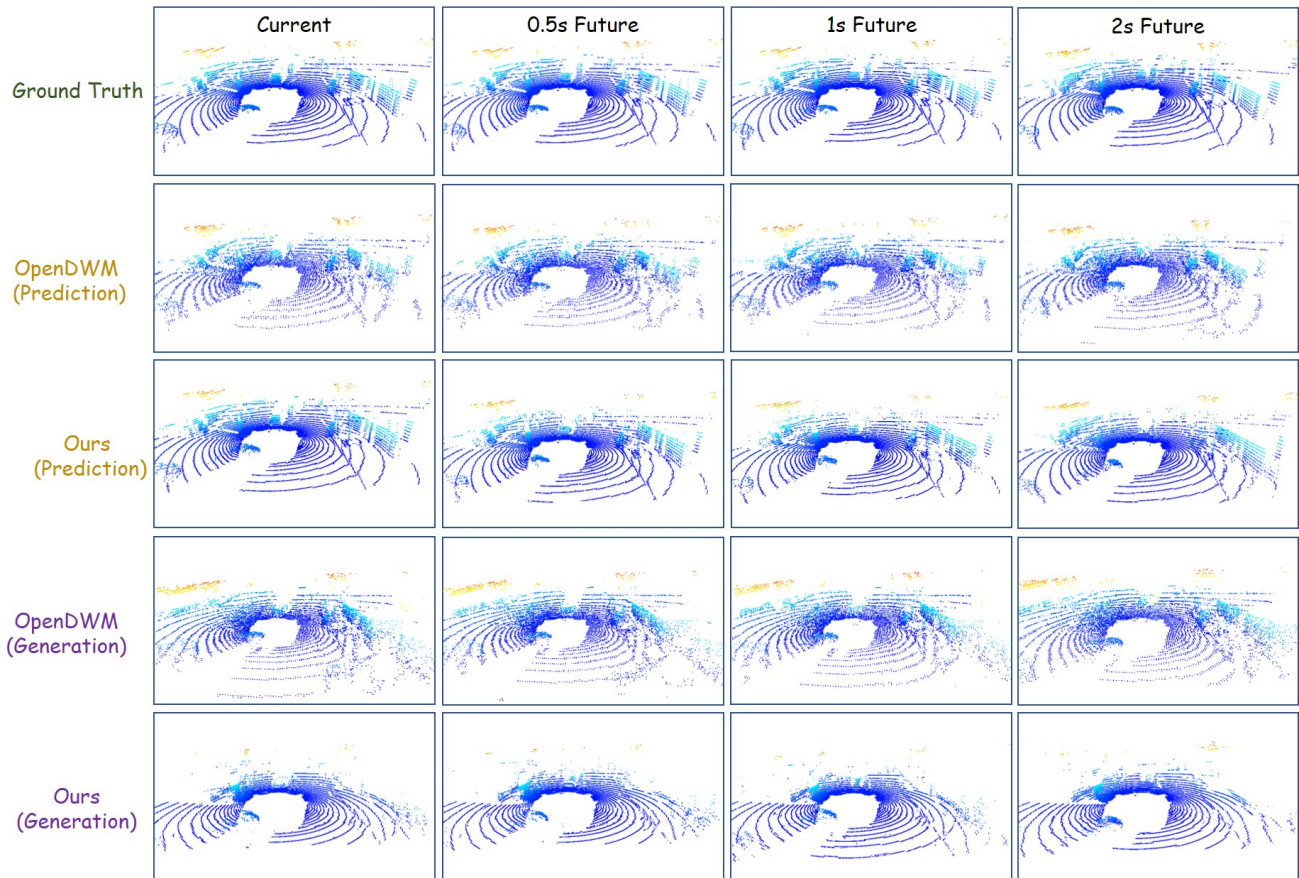


Figure 8. Qualitative results for prediction and generation. We compare our method with OpenDWM against the ground truth for future horizons up to 2s. Our method consistently produces sharper and more accurate results for both static background and dynamic objects (highlighted) compared to the baseline. The baseline’s predictions and generations degrade significantly over time, losing structural detail.